Materials Advances

Accepted Manuscript

This article can be cited before page numbers have been issued, to do this please use: J. Yadav, S. P. Vanam, S. K. Parate, N. Doddi, V. Srihari, V. Pralong, M. Fichtner and P. Barpanda, *Mater. Adv.*, 2025, DOI: 10.1039/D5MA00455A.

ROYAL SOCIETY OF CHEMISTRY

rsc.li/materials-advances

View Article Online
DOI: 10.1039/D5MA00455A

Effect of Ti-doping on Electrochemical Activity of $Li_{0.44}MnO_2$ Cathode Material for Li-ion Batteries

Jaya Yadav,[a] Sai Pranav Vanam,[a] Shubham K. Parate,[b] Nikhil Doddi,[a] Velaga Srihari,[c] Valérie Pralong,[d,e] Maximilian Fichtner,[f,g] Prabeer Barpanda*[a,f,g]

[a]Faraday Materials Laboratory (FaMaL), Materials Research Center, Indian Institute of Science, Bangalore 560012, India

[b]Centre for Nano Science and Engineering (CeNSE), Indian Institute of Science (IISc), Bangalore 560012, India

[c]Synchrotron Utilization Section, Raja Ramanna Centre for Advanced Technology, Indore 452013, India

[d]Normandie University, ENSICAEN, UNICAEN, CNRS, CRISMAT, Caen 14000, France

[e]Réseau sur le Stockage Electrochimique de l'Énergie (RS2E), Amiens, France

[f]Helmholtz Institute Ulm (HIU), Electrochemical Energy Storage, Ulm 89081, Germany

[g]Institute of Nanotechnology (INT), Karlsruhe Institute of Technology (KIT), Karlsruhe 76021, Germany

* Corresponding author : prabeer@iisc.ac.in

View Article Online
DOI: 10.1039/D5MA00455A

Abstract

Manganese-based oxides can work as economic cathode materials for Li-ion batteries. Various metastable manganese oxides can exhibit efficient Li^+ (de)insertion activity. One such system is chemically derived $Li_{0.44}MnO_2$ offering reversible Li^+ intercalation involving Mn^{4+}/Mn^{3+} redox reaction albeit with poor rate kinetics. In this work, the electrochemical activity of tunnel-structured $Li_{0.44}MnO_2$ has been enhanced by tailoring its crystal structure and particle morphology by Ti-doping into Mn sites. X-ray diffraction and spectroscopy analyses revealed successful Ti-doping while retaining the original structure. Varied degree of Ti-doping was found to exhibit improved electrochemical performance, with the $Li_{0.44}Mn_{0.89}Ti_{0.11}O_2$ delivering the highest capacity of 129 mAh g^{-1} at a rate of C/20. Ti-doping was further found to improve the Li^+ diffusivity and rate kinetics. This enhancement in electrochemical activity can be ascribed to the combined effect of Ti-induced lattice expansion and decrease in particle size. Electrochemical titration and ex situ analyses revealed the occurrence of single-phase (solid-solution) redox mechanism. Ti-doped $Li_{0.44}MnO_2$ can be harnessed as an economic cathode for Li-ion batteries.

Keywords: Li-ion batteries, $Li_{0.44}MnO_2$, tunnel-type cathodes, Ti-doping, Li^+ diffusion, capacity retention

1. Introduction

Since their commercialization in 1990s by SONY®, Li-ion batteries are widely being used in sectors ranging from variety of small-scale consumer electronics to large-scale (hybrid) electric vehicles and grid storage. Cathodes form a key player dictating the net cost and performance of batteries, thus driving exploration of design and development of efficient cathode frameworks. While Co- and Ni-based oxides rule the commercial battery sector, there is growing need to

View Article Online
DOI: 10.1039/D5MA00455A

develop low-cost cathodes from earth-abundant elements (like Fe or Mn). Mn-based oxides are particularly attractive due to their large number of advantages in terms of less toxicity, tunable redox potential owing to variable oxidation states, and structural diversity/polymorphism.[1,2]

Bruce et al. reported one such composition $LiMnO_2$ layered oxide delivering a high initial capacity of >200 mAh g^{-1} even at the high current density of 0.5 mA cm^{-2}. However, the capacity retention was poor over cycling.[3] Other than layered oxides, spinel-structured $LiMn_2O_4$ also have been exploited as a cathode, but suffers from fast capacity decay at elevated temperatures (ca. T> 55 °C) in acidic electrolytes.[4] Armstrong et al. reported Li_xMnO_2 possessing tunnel structure with excellent capacity retention in the voltage window of 2.8-3.6 V, but the capacity was limited to 80-85 mAh g^{-1} at a current density of 0.5 mA cm^{-2}. In contrast to spinel $LiMn_2O_4$, this material showed remarkable cyclability at high temperatures of 85 °C and without any layer-to-spinel phase transformation unlike many layered oxides.[5,6] Glycine-nitrate combustion synthesized Li_xMnO_2 (GNP-Li_xMnO_2) demonstrated better rate capability than solid-state synthesized Li_xMnO_2 (SS-Li_xMnO_2).[6] Despite numerous attempts to improve the electrochemical activity of $Li_{0.44}MnO_2$ via different synthesis techniques and structural modification, additional enhancements are needed to ensure its suitability for potential applications. Also, Mn-based cathode materials suffer from Jahn-Teller distortion, which affects their cycling stability. Ion substitution has been proven to be an efficient strategy to enhance the electrochemical properties in terms of capacity, cycling stability, rate performance, and preventing phase transformations by tuning the crystal structure.[7–9] For example, substituting Li with Ca increased capacity retention.[10] Similarly, partial substitution of Mn with Ti was found to enhance long-term capacity retention and to mitigate material dissolution.[11-13] A two-fold increase in capacity was observed when additional lithium was inserted

View Article Online
DOI: 10.1039/D5MA00455A

by molten $LiNO_3$-LiOH at a low temperature.[14] Hence, tunnel-structured Li_xMnO_2 forms a promising compound for low-cost energy storage applications.

Li_xMnO_2, having tunnel-type crystal structure, has five different crystallographic Mn sites, with MnO_6 octahedra and MnO_5 polyhedra forming two types of tunnels. Li1 resides in the pseudohexagonal smaller tunnel, while Li2 and Li3 occupy larger S-shaped tunnel sites.[5] Till date, all reports on Li_xMnO_2 systems were mostly conducted in the voltage window of 2.5 ~ 4.8 V. But, high voltage (ca. > 4.6 V) cycling is usually associated with electrolyte degradation or triggering of anion redox, resulting in large voltage hysteresis and rapid capacity fading when carbonate electrolytes are used.[15,16] The electrochemical performance of tunnel structured Li_xMnO_2 can be improved with Ti substitution that involves multiple factors including the synthesis protocols, cell configuration, structural modification and appropriate electrolyte etc.[17] Herein, we have tuned the degree of Ti-substitution and operational window to obtain chemically derived $Li_{0.44}Mn_{1-x}Ti_xO_2$ with optimum electrochemical performance. The role of Ti-substitution on lattice modification and diffusion rate kinetics has been investigated along with the underlying solid-solution redox mechanism upon Li^+ (de)insertion.

2. Experimental section

2.1. Material synthesis. Pristine and Ti-doped $Li_{0.44}Mn_{1-x}Ti_xO_2$ (x = 0, 0.11, 0.22, 0.33, 0.44, 0.56) powders were obtained by conventional solid-state synthesis of their Na analogues followed by Na-Li ion-exchange involving molten salt.[12] First, stoichiometric amounts of $NaNO_3$ (99.7%, Sigma), $MnCO_3$ (99%, Alfa Aesar), and TiO_2 (99.8%, Alfa Aesar) were intimately mixed for 20 minutes using agate mortar and pestle. These precursor mixtures were calcined at 900 °C for 6 h (heating rate = 5 °C/min) in a muffle furnace (in air) to yield $Na_{0.44}Mn_{1-x}Ti_xO_2$ (x = 0, 0.11, 0.22,

View Article Online
DOI: 10.1039/D5MA00455A

0.33, 0.44, 0.56) products. A starting ratio of Na/(Mn+Ti) = 0.5 was taken to compensate for Na loss at high temperature. Following, ion exchange reaction was carried out by mixing the Na-based $Na_{0.44}Mn_{1-x}Ti_xO_2$ oxides with a eutectic combination of $LiNO_3$ (88 mol %) and LiCl (12 mol %) that was calcined at 300 °C for 10 h (heating rate = 5 °C/min) in a muffle furnace (in air) to obtain the target $Li_{0.44}Mn_{1-x}Ti_xO_2$ compounds.

2.2. Material characterization. The crystal structure was characterized by X-ray powder diffraction with a PANalytical X'pert pro diffractometer equipped with a Cu Kα source (λ_1 = 1.5405 Å, λ_2 = 1.5443 Å) operating at 40 kV/30 mA. The diffractograms were collected in the 2θ range of 5−80° with a scanning step of 0.026° in Bragg−Brentano geometry. Synchrotron XRD patterns were acquired at the BL-11 beamline at the Indus-2 synchrotron facility (Raja Ramanna Centre for Advanced Technology, Indore, India) with a beam wavelength of 0.7305 Å. Rietveld refinement was performed using the Fullprof suite program.[18] Linear interpolation and pseudo-Voigt functions were used for the background and shape fitting, respectively. The crystal structure was illustrated with the VETSA software.[19]

The particle morphology was examined using high-resolution scanning electron microscopy (Ultra 55 FESEM Carl Zeiss EDS, operating at 5−20 kV) and transmission electron microscopy (Thermo Fisher Titan Themis, operating at 300 kV). X-ray photoelectron spectroscopy surface analysis was carried out with a Thermo Scientific K_α XPS instrument with an incident monochromated X-ray beam from the Al target (accelerating voltage = 12 kV, emission current = 6 mA). Shift corrections were done by taking carbon as reference at binding energy of 284.6 eV. Magnetic susceptibility was measured with a Quantum Design MPMS XL SQUID magnetometer in a DC field in the temperature range of 2~400 K in zero-field-cooled (ZFC) mode. Fourier-

View Article Online
DOI: 10.1039/D5MA00455A

transform infrared spectroscopy (FTIR) was conducted with a PerkinElmer (Frontier) instrument using transmission mode in the wavenumber window of 400-7800 cm^{-1}. Raman spectra were acquired with a LabRAM HR unit (Horiba Jobin Yvon) using a 532 nm (green) laser as the excitation source.

For post-mortem analysis, the samples were recuperated at different states of (dis)charge of electrochemical cycling at a rate of C/40. The cathodes were cycled using coin-type (CR-2032) or Swagelok cells as described below. Afterwards, the cells were disassembled, the electrodes were washed with propylene carbonate and dried before various material characterizations.

2.3 Electrochemical characterization. The working electrodes were prepared by intimately mixing the as-synthesized active material, super P-carbon black, and polyvinylidene fluoride (PVDF) in proportions of 80:10:10 (w/w/w) in N-methyl-2-pyrrolidone (NMP). This slurry was coated uniformly on Al foil by a doctor blade and was dried at 80 °C overnight in a vacuum oven. The active mass loading was 2-4 mg cm^{-2}. CR2032 type coin cells were assembled in an Ar-filled glovebox (MBraun LABstar glovebox with H_2O/O_2 level of <0.5 ppm). Metallic Li foil was used as counter and reference electrodes for the Li-ion half-cells. The separation between working and counter electrodes was maintained by a glass microfiber filter (Whatman, grade GF/C) saturated with a commercial electrolyte comprising of 1 M $LiPF_6$ in ethylene carbonate (EC)/diethyl carbonate (DEC)/dimethyl carbonate (DMC) (1:1:3 (v/v)) (Sigma Aldrich). Galvanostatic (dis)charge tests were conducted in the voltage window of 2-4 V (vs. Li^+/Li) (at 25 °C) using a Neware BTS-4000 battery tester. Cyclic voltammetry (CV) at different scan rates (from 0.1~ 1 mV/s), potentiostatic intermittent titration technique (PITT) at a rate of C/50 and galvanostatic intermittent titration technique (GITT) at a rate of C/20 were performed using a Bio-Logic BCS

View Article Online
DOI: 10.1039/D5MA00455A

805/810 automatic battery cycler. Electrochemical impedance spectroscopy (EIS) was performed in the frequency range of 10 mHz-200 kHz using a Bio-Logic SP300 workstation.

3. Results and discussion

While solid-state route often yields thermodynamically stable polymorphs/phases, numerous soft chemistry methods (involving two or more steps) can be adopted to stabilize various metastable (intermediate) phases often exhibiting superior materials properties and performance. The layered structured LiT_MO_2 (T_M = 3*d* metals) oxides can be obtained by direct high-temperature synthesis. On the other hand, the formation of tunneled structure Li_xMnO_2 needs a two-step soft chemistry protocol. Here, the target pristine and Ti-doped $Li_{0.44}Mn_{1-x}Ti_xO_2$ (x = 0, 0.11, 0.22, 0.33, 0.44, 0.56) phases were prepared by molten salt ion-exchange using their Na-analogues as starting materials.[12] The scheme for this two-step synthesis is depicted in **Figure 1**a. With higher degree of Ti-doping, the colour of powder samples changed from black to brown. The phase purity of pristine $Li_{0.44}MnO_2$ (now onwards referred as LMO1) was verified by Rietveld refinement of synchrotron XRD pattern (**Fig. S1**). Phase-pure LMO1 was obtained assuming an orthorhombic crystal structure with *Pbam* symmetry. The detail lattice parameters and lattice coordinates are given in **Table S1**. Following, the diffraction patterns of various Ti-doped samples were analyzed. As shown in Figure 1b, all major diffraction peaks of all compositions can be indexed to the orthorhombic crystal system (isostructural to LMO1). Minor amount of Mn_2O_3 peaks were also observed, which is a thermodynamically stable phase.[20,21] When the Ti concentration was over 0.22, it led to the formation of minor amount of $Li_2Ti_6O_{13}$ impurity phase.[22] Higher degree of Ti-doping led to shifting of XRD peaks to lower 2θ values, indicating the steady rise in *d*-spacing (i.e. lattice expansion). The typical crystal structure of this tunnel type oxide is illustrated in Figure 1c.

View Article Online
DOI: 10.1039/D5MA00455A

There are 5 crystallographically distinct Mn sites with different oxidation states. While Mn1 and Mn2 are in the +3 oxidation state, the rest (Mn3, Mn4 and Mn5) are in the +4 oxidation state.

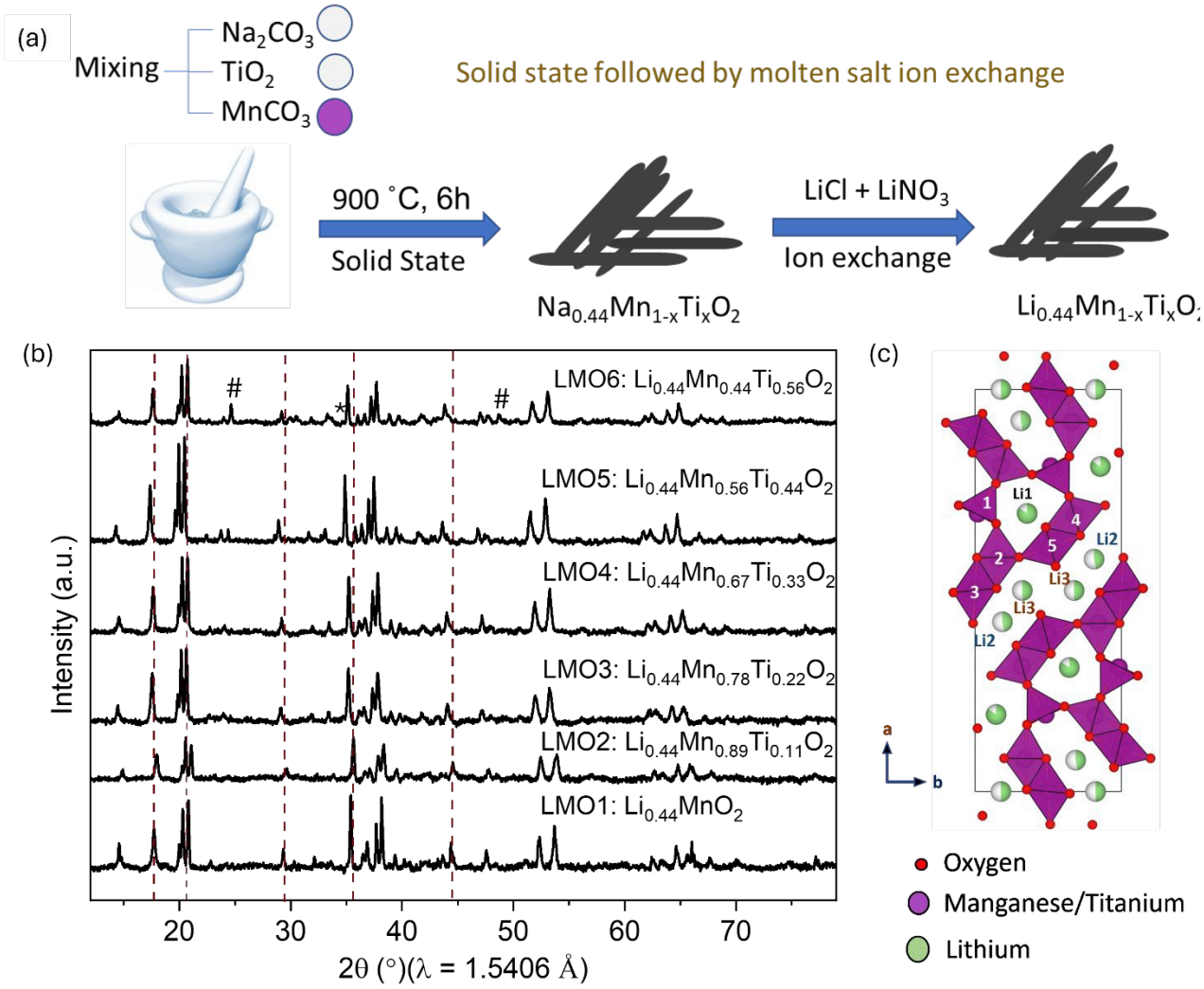

Figure 1. (a) Scheme for the material synthesis involving solid-state route followed by molten salt ion exchange. (b) Comparative XRD patterns of tunnel-type $Li_{0.44}Mn_{1-x}Ti_xO_2$ ($0 \leq x \leq 0.56$) oxide compositions. The vertical dashed lines are shown as guide to eyes to illustrate steady peak shifting upon Ti-doping. (* Mn_2O_3, # $Li_2Ti_6O_{13}$) (c) Structural illustration of $Li_{0.44}Mn_{1-x}Ti_xO_2$ oxide involving large tunnels. The constituent MO_6 octahedra and MO_5 polyhedra (M = Mn/ Ti) are shown in pink delimiting tunnels accommodating partially occupied Li sites (green/white spheres). Constituent Mn occupies 5 distinct sites as indicated by numbers inside pink polyhedra.

View Article Online
DOI: 10.1039/D5MA00455A

The size of Ti^{4+} ion is 0.68 Å, which is comparable to that of the isovalent Mn^{4+} ion (0.60 Å).[11] Hence upon doping, Ti^{4+} most likely occupy the Mn^{4+} sites (at low concentration of Ti). Even with higher degree of Ti doping, Ti^{4+} does not enter Mn1 sites having square pyramidal geometry.[23] To probe the sites occupied by Ti, synchrotron XRD study was conducted for $Li_{0.44}Mn_{0.89}Ti_{0.11}O_2$ (here onwards referred as LMO2). The corresponding Rietveld refinement and crystal structure are shown in **Figure 2**. The lattice parameters and coordinates are listed in **Table S2** and **Table S3**. Ti was found to majorly occupy Mn4 and Mn5 sites as illustrated in Figure 2b and led to the expansion in lattice parameters and unit cell volume (Table S3). In addition to diffraction, magnetic properties can be gauged for detecting structural defects and compositional changes in battery materials containing 3*d* transition elements. Figure 2c compares the magnetic susceptibility behaviour of the pristine (LMO1) and Ti-doped $Li_{0.44}Mn_{0.89}Ti_{0.11}O_2$ (LMO2) and $Li_{0.44}Mn_{0.44}Ti_{0.56}O_2$ (LMO6) compositions. In case of pristine LMO1, a clear paramagnetic to antiferromagnetic transition was observed around $T_N \sim 9$ K. However, upon Ti^{4+} doping into the structural framework, the replacement of Mn^{4+}/ Mn^{3+} ions by nonmagnetic Ti^{4+} ion (which has d^0 configuration) decreased the exchange interactions between Mn^{4+}–O–Mn^{4+}/Mn^{3+}.[24,25] Thus, upon gradual Ti-doping, a decrease in antiferromagnetic exchange interactions was noticed with no sharp transition points. This further attests successful Ti-doping into the lattice framework. Following, the presence of Ti was probed with XPS spectroscopy. Figure 2d shows the wide range core XPS survey spectra of LMO1 and LMO2. Characteristic Ti 2*p* peak was noticed in LMO2, which was absent in the case of LMO1. Further, FTIR spectra of different Ti-doped compositions are illustrated in **Figure S2**. In addition to the bands related to Mn–O and Mn–O–Mn stretching/bending modes, the gradual doping of Ti led to appearance of peaks corresponding to

View Article Online
DOI: 10.1039/D5MA00455A

O–Ti–O bending and Ti–O asymmetric stretching.[26] Overall, Ti-doping was confirmed by various diffraction and spectroscopy tools.

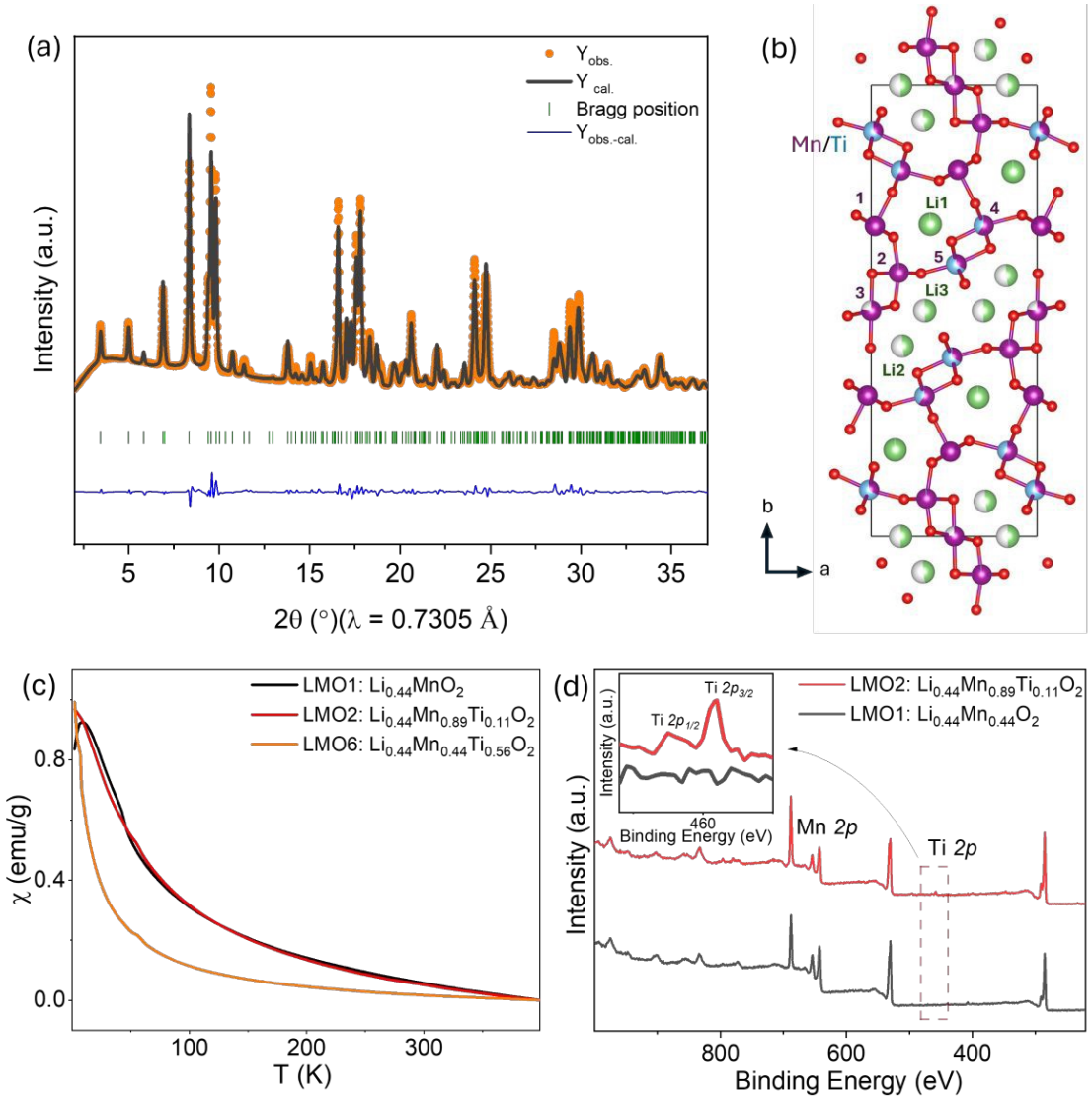

Figure 2. (a) Rietveld refined synchrotron XRD pattern (λ = 0.7305 Å) of $Li_{0.44}Mn_{0.89}Ti_{0.11}O_2$ (LMO2). The experimental data points (yellow dots), simulated pattern (black line), their difference (blue line) and Bragg diffraction peaks (green ticks) are shown. (b) Corresponding crystal structure is shown comprising of Mn/Ti octahedra (Mn in purple and Ti in blue spheres) and Li (green spheres). (c) Comparative magnetic susceptibility plots of LMO1, LMO2 and LMO6. (d) Wide XPS survey spectra of pristine (LMO1) and Ti-doped $Li_{0.44}MnO_2$ (LMO2). (Inset displaying Ti 2*p* peak in LMO2).

View Article Online
DOI: 10.1039/D5MA00455A

The ion-exchange produced LMO1 with rod-like micrometric morphology grown along c-direction (**Figure 3**a,b). The corresponding HRTEM and SAED patterns revealed crystalline nature. Uniform elemental distribution was captured by HAADF-STEM elemental mapping as shown in **Figure S3**. LMO2 also exhibited morphology with rods growing along [001] direction (Figure 3e,f). Uniform Ti-doping was revealed by elemental mapping with expected atomic fraction (**Figure S4**). The diffraction spots observed in the SAED pattern (Fig. 3g) confirmed the tunnel-type orthorhombic structure. From HRTEM images, an increase in the *d*-spacing of the (200) plane was observed for LMO2 (0.4493 nm) as compared to LMO1 (0.4438 nm) (Fig. 3d,h). All Ti-doped oxide samples had similar morphology (**Figure S5**). However, upon gradual increase in Ti concentration, the length of the rods along the c-direction became shorter. Following successful synthesis, the effect of Ti-doping on electrochemical activity was investigated.

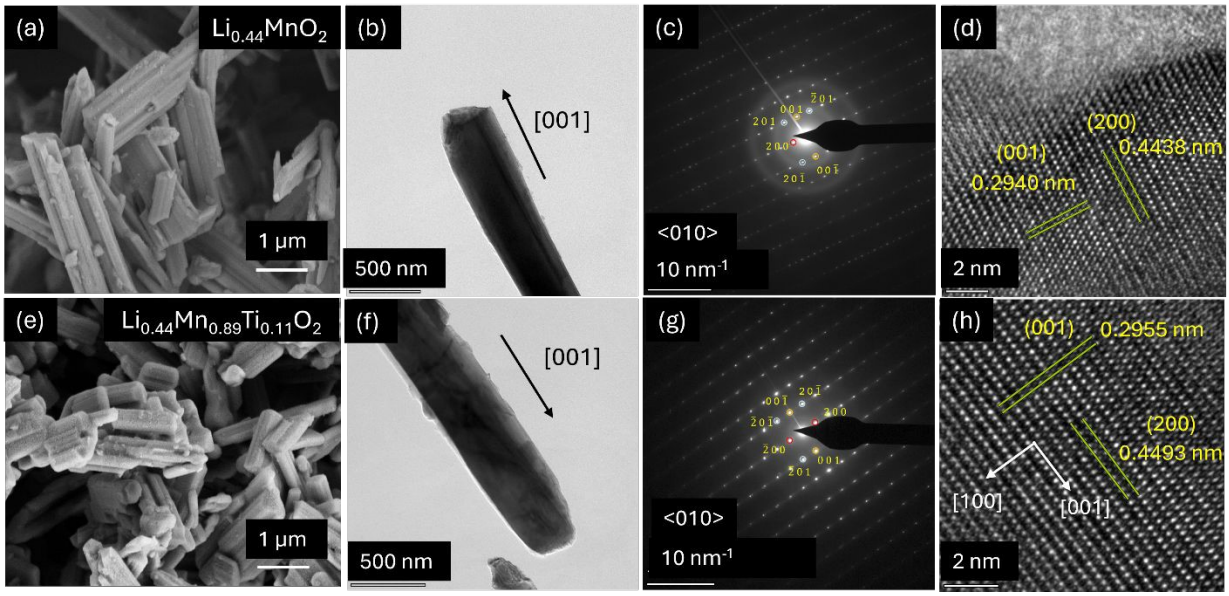

Figure 3. Morphology analysis. (a,e) SEM images of $Li_{0.44}MnO_2$ (LMO1) and $Li_{0.44}Mn_{0.89}Ti_{0.11}O_2$ (LMO2). (b,c,d) TEM image, SAED pattern and HRTEM image of LMO1. (f,g,h) TEM image, SAED pattern and HRTEM image of LMO2. <010> zone axis was taken for the SAED patterns.

View Article Online
DOI: 10.1039/D5MA00455A

Galvanostatic (dis)charge capacity of all Ti-doped compositions was evaluated using as-synthesized active materials without any further cathode optimization. The corresponding profiles of cells, cycled in the potential window of 2-4 V (at C/20 rate), are shown in **Figure 4** and **Figure S6**. The respective differential voltage (dQ/dV) profiles are given in **Figure S7**. The pristine $Li_{0.44}MnO_2$ exhibited a multistep voltage profile involving Mn^{4+}/Mn^{3+} redox activity centered at 3.2 V (vs. Li/Li^+). Ti-doping led to increase in capacity for LMO2 exhibiting the highest first discharge capacity of 128 mAh g^{-1}. This increase in electrochemical activity can be rooted to the ease of Li^+ (de)intercalation owing to Ti-induced structural expansion. While Li^+ (de)insertion primarily occurs from larger Li2 and Li3 sites (Fig. 1c), upon Ti-doping, Li1 site can become accessible due to lattice expansion. Hence, LMO2 exhibited enhanced capacity. Higher degree of Ti-doping led to steady decrease in capacity (Fig. S6) due to lower amount of electroactive species (Mn^{4+}). Also, the voltage profiles became slopier with progressing Ti doping with average redox activity centered around 3.2 V.

A comparison of the rate performance of LMO1 and LMO2 is displayed in Figure 4c. The Ti-doped LMO2 delivered reversible capacity of 129.4, 115.6, 98, and 73 mAh g^{-1} at C/20, C/10, C/5 and C/2, respectively, which were higher than pristine LMO1 at the respective rates. The superior rate kinetics in LMO2 can be rooted to its larger lattice size stemming from Ti-doping. In addition to higher capacity and rate kinetics, Ti-doping was also found to enhance the cycling stability (Fig. 4a,b). Fast cycling was performed at 2C rate (Figure 4d). LMO2 showed better capacity retention of 85.2% after 50 cycles with stable coulombic efficiency. It can be due to the decrease in the number of Jahn-Teller active Mn^{3+} species.[27] Also, the bond energy of Ti–O (662 kJ/mol) is significantly higher than that of Mn–O (402 kJ/mol). This strong Ti–O bond can stabilize the structure by mitigating substantial bond changes in the Mn^{4+}–O bond within the

View Article Online
DOI: 10.1039/D5MA00455A

octahedral environment. This stabilization occurs because oxygen atoms are shared between Mn^{3+}/Mn^{4+} and Ti^{4+} during the transition metal redox process.[22] A comparison with previously reported tunnel-type and spinel manganese oxides (**Table 1**) highlights that this material achieves higher or comparable retention relative to other doped tunnel-type oxides, including Ca- and Ti-substituted variants. This establishes Ti^{4+} doping as an effective strategy to enhance the long-term stability of tunnel-type Mn-based cathodes.

Overall, considering the optimal balance between the reversible capacity and cycling stability related to Mn^{3+} species, LMO2 was found to offer best electrochemical activity and was considered for further studies. To optimize the voltage window, the electrochemical performance was tested at different voltage window (**Figure S8**). Optimum electrochemical activity was noticed within 2-4 V window. Thus, further mechanistic studies were conducted for LMO2 sample in the optimized voltage window of 2-4 V.

Table 1. Comparison of cycling performance for Ti-doped and undoped tunnel/spinel-type Mn-based cathode materials.

Material	Structure	Retention	Conditions	Reference
$Li_{0.44}MnO_2$ (pristine)	Tunnel (*Pbam*)	~70–72% after 150 cycles	0.5 mA/cm^2 (2 - 3.6 V)	5
$Na_{0.44}Mn_{0.89}Ti_{0.11}O_2$ (Ti-doped $Na_{0.44}MnO_2$)	Tunnel (*Pbam*)	~79% after 600 cycles	1C (2 - 3.8 V)	22
$Li_{0.27}Na_{0.007}Ca_{0.03}MnO_2$ (Ca-substituted $Li_{0.44}MnO_2$)	Tunnel (*Pbam*)	85% after 50 cycles	30 mA/g (2 – 4.8 V)	10
$LiMn_{1.97}Ti_{0.03}O_4$ (Ti doped $LiMn_2O_4$)	Spinel (*F-d*3*m*)	~81.65% after 100 cycles	0.5C (2.9 - 4.3 V)	28
$Li_xMn_{0.89}Ti_{0.11}O_2$ (Ti-substituted $Li_{0.44}MnO_2$)	Tunnel (*Pbam*)	85.2% after 50 cycles	2C (2 - 4 V)	This work

View Article Online
DOI: 10.1039/D5MA00455A

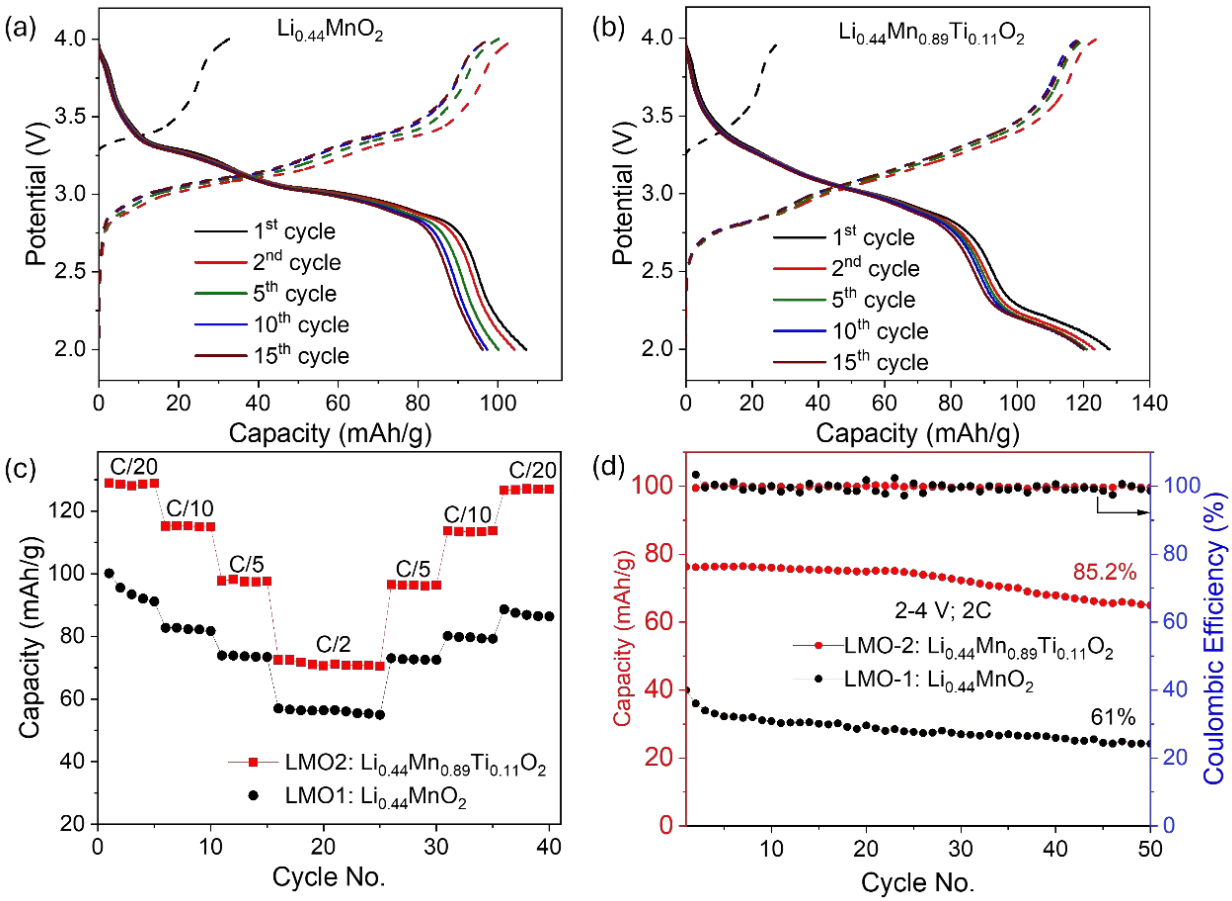

Figure 4. Galvanostatic charge/discharge profiles for (a) pristine $Li_{0.44}MnO_2$ (LMO1) and (b) Ti-doped $Li_{0.44}Mn_{0.89}Ti_{0.11}O_2$ (LMO2) composition cycled at a rate of C/20 (2-4 V). (c) Corresponding rate kinetics for LMO1 and LMO2. (e) Cycling stability and coulombic efficiency of LMO1 and LMO2 at cycled at a fast rate of 2C in the voltage window of 2-4 V.

View Article Online
DOI: 10.1039/D5MA00455A

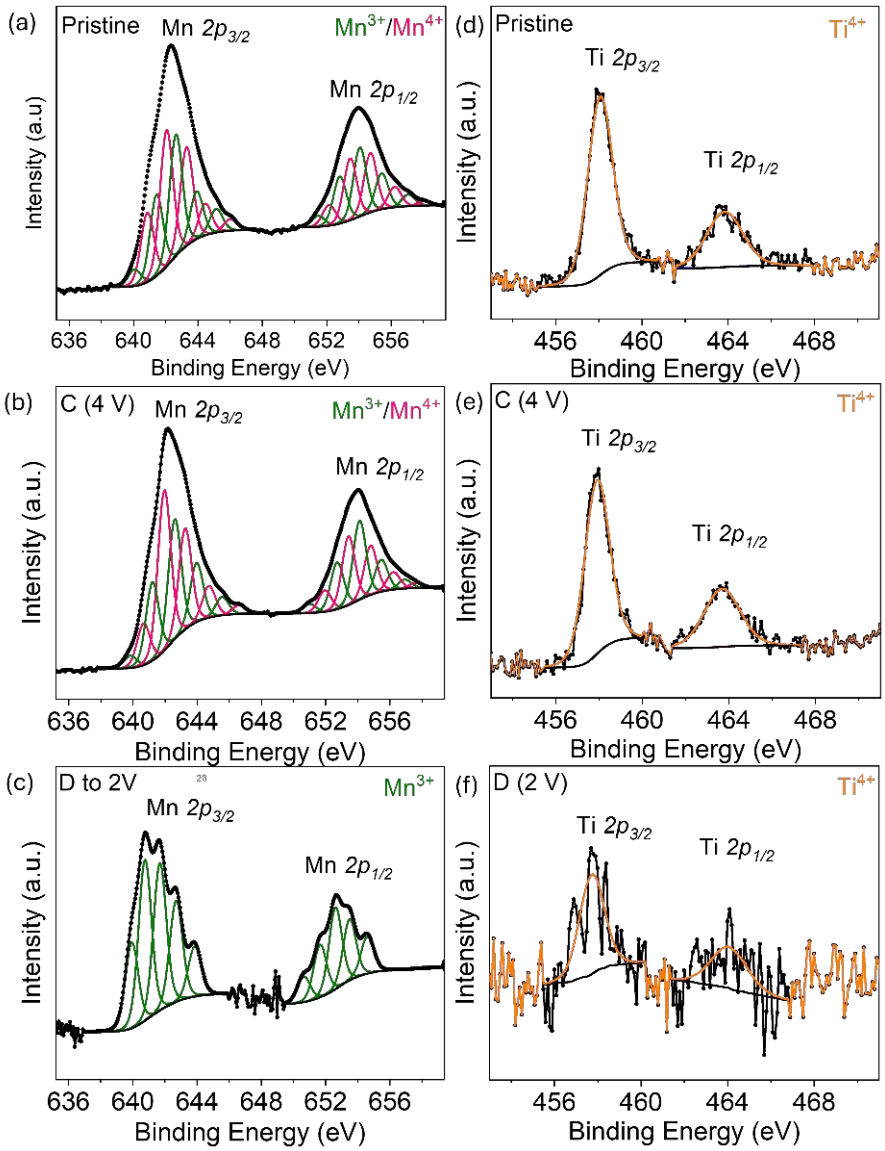

Figure 5. Mn 2*p* XPS Spectra of LMO2: (a) Pristine cathode, (b) Charged to 4 V, and (c) Discharged to 2 V. Mn^{4+}/Mn^{3+} redox states are captured. Ti 2*p* XPS spectra of LMO2: (d) Pristine state, (e) Charged to 4 V, and (f) Discharged to 2 V. Ti^{4+} redox state remains unaltered.

The charge compensation mechanism during Li^{+} (de)insertion was analyzed by ex situ X-ray photoelectron spectroscopy (XPS). In the pristine LMO1, the (de)lithiation occurred involving Mn^{4+}/Mn^{3+} redox activity as shown in **Figure S9**. The ex situ XPS spectra of Ti-doped LMO2 are shown in **Figure 5**. The Mn 2*p* and Ti 2*p* XPS spectra were fitted using curve-fitting modes, as

View Article Online
DOI: 10.1039/D5MA00455A

reported earlier.[29,30] Due to spin-orbit coupling, Mn 2*p* spectra split into Mn $2p_{1/2}$ peak, centred at 653.96 eV and Mn $2p_{3/2}$ at 642.3 eV. From the deconvoluted Mn 2*p* spectra, Mn was found to have mixed oxidation states of Mn^{3+} and Mn^{4+}, similar to LMO1. Ti 2*p* split into two peaks: one with a peak value of 463.8 eV corresponding to the Ti $2p_{1/2}$ and another peak at 458 eV corresponding to the Ti $2p_{3/2}$. This indicates the existence of the Ti^{4+} in LMO2. When LMO2 was charged to 4 V, the Mn 2*p* spectra still exhibited a mixed oxidation state, but with a higher ratio of Mn^{4+}/Mn^{3+} indicating the oxidation of some Mn^{3+} to Mn^{4+} upon charging. When the LMO2 was discharged to 2 V, the Mn 2*p* spectra solely showed the existence of Mn^{3+}, indicates complete reduction of Mn^{4+} to Mn^{3+} after discharge. The oxidation state of Ti remained unaltered ruling out any Ti redox during cycling. Hence, only Mn^{4+}/Mn^{3+} redox activity compensates for Li^+ (de)insertion.

To probe the structural evolution during cycling, ex situ XRD was conducted at various states of (dis)charge as illustrated in **Figure 6**a and **S10**. The tunnel structure with the orthorhombic crystal system was maintained at all states of charge during cycling. A small shift was observed towards the lower angle after fully discharging to 2 V indicating lattice expansion due to more Li^+ insertion. A solid-solution redox process was confirmed without any phase transformation. Even after 1000 cycles conducted at fast rate of 2C, the tunnel structure was maintained (**Figure S11**). The reversibility of this material was observed via ex situ Raman spectroscopy capturing localized structural alterations (Figure 6b). All Raman bands were unaltered post cycling. Ex situ TEM study was employed to probe structural evolution (Figure 6c). Upon charging to 4 V and discharging to 2 V, the tunnel structure and rod-like morphology were maintained within an orthorhombic crystal system. Minor changes in the *d*-spacing of planes, particularly in the (200) plane, were observed that comes back to pristine structure upon discharging.

View Article Online
DOI: 10.1039/D5MA00455A

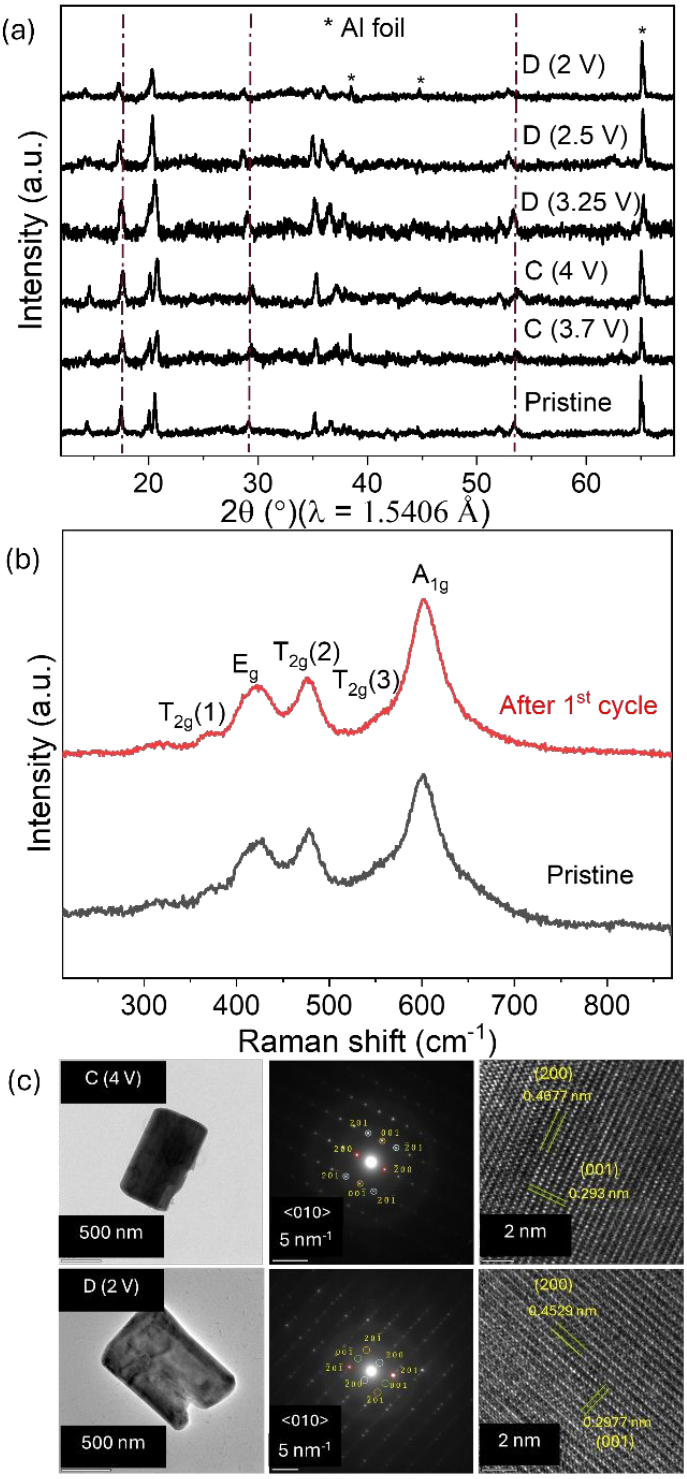

Figure 6. (a) Ex situ XRD patterns of LMO2 at different states of charge. (b) Comparative Raman spectra of LMO2 at pristine and after 1st cycle. (c) Ex situ TEM, SAED and HRTEM analysis of LMO2 cathode charged to 4 V (top) and discharged to 2 V (bottom). <010> zone axis was taken for the SAED patterns.

View Article Online
DOI: 10.1039/D5MA00455A

Following, the Li^+ (de)insertion mechanism was elucidated by potentiostatic intermittent titration technique (PITT) at a rate of C/50 in 2-4 V range (**Figure 7**a). "Cottrel-type" *I-t* behaviour was observed, indicating a monophase mechanism in accordance with the ex situ XRD results.[31] The rate kinetics was examined using galvanostatic intermittent titration technique (GITT) and chemical diffusion coefficients were calculated for LMO1 and LMO2 (Figure 7b and **Figure S12**). The Ti-doped LMO2 exhibited higher diffusion coefficient values compared to LMO1, which corroborates the rate performance results. The diffusion coefficient values varied between 1.8 x 10^{-11} – 2.08 x 10^{-10} and 6.367 x 10^{-11} – 1.2 x 10^{-11} cm^2 s^{-1} for the LMO2 and LMO1 respectively during cycling. The diffusion coefficient values were smaller during discharge than the charge. These values fall well within the range reported by Saint et al. for tunnel-type Mn oxide, particularly in the voltage regime dominated by larger tunnels.[17] In addition, electrochemical impedance spectroscopy (EIS) measurements after 1st cycle (C/20) for both LMO1 and LMO2 were performed. Nyquist plots for both undoped and Ti-doped $Li_{0.44}MnO_2$ (**Figure S13**) show a typical semicircle in the high-frequency region and a sloped tail at low frequencies. The Ti-doped sample exhibits a noticeably smaller semicircle diameter, indicating reduced charge-transfer resistance (R_{ct}). This suggests improved interfacial kinetics and faster Li^+ transport. A similar trend was reported for Ti-doped $Na_{0.44}MnO_2$, where the fitting of the EIS data also revealed a decrease in R_{ct} upon Ti substitution.[8] It further affirms that Ti^{4+} enhances electrochemical performance by improving charge transport and stabilizing the electrode–electrolyte interface.[32]

The enhanced rate performance observed in the Ti-doped material can be attributed to the reduced size of rod-shaped particles, leading to higher diffusion coefficients. Here, Ti^{4+} ions are not actively engaged in electrochemical reactions within the 2-4 V range. However, their inclusion triggers an expansion in the unit cell volume, facilitating more efficient (de)intercalation of Li^+

View Article Online
DOI: 10.1039/D5MA00455A

ions. Consequently, a slight Ti doping enhances the capacity. Nevertheless, excessive Ti doping reduces the presence of electrochemically active Mn ions. Moreover, Ti^{4+} substitution at Mn^{3+} sites suppresses Jahn-Teller distortion during repeated cycling, thereby improving capacity retention. Apart from Ti dopant concentration, the operating potential window can affect the net electrochemical performance. To gauge the effect of potential window, LMO2 was cycled to voltage ranging from 4.8 V to 1 V as shown in **Figure S14**. The ex situ XPS spectra of Mn 2*p* and Ti 2*p* (at discharge to 1 V) are presented in **Figure S15**. While Ti is redox inactive throughout the voltage window, extra capacity arises by triggering Mn^{3+} to Mn^{2+} redox process at voltage below 2 V. Thus, using a wider voltage window can activate (i) anionic redox at high voltage (ca. >4.5 V) and (ii) multiple cationic redox (Mn^{4+}/Mn^{3+} and Mn^{3+}/Mn^{2+}) at low voltage that can yield high capacity and energy density in Ti-doped $Li_{0.44}MnO_2$ that warrants a detail study in future.

View Article Online
DOI: 10.1039/D5MA00455A

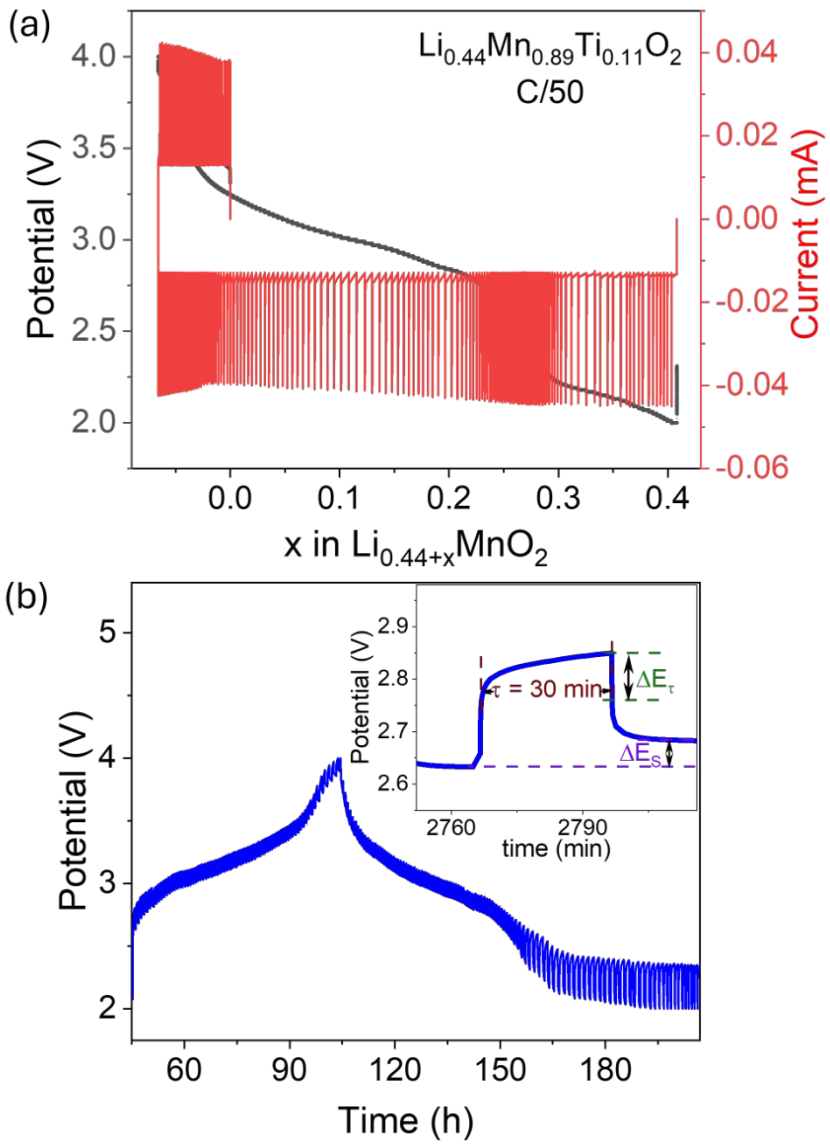

Figure 7. (a) PITT curve of LMO2 cycled at a rate of C/50 (2-4 V). (b) Voltage profile of LMO2 during GITT (Current was provided for 30 mins at C/20 rate followed by rest for 1h). Inset shows expansion of the single titration curve.

4. Conclusions

In summary, metastable Ti-doped $Li_{0.44}MnO_2$ compositions with orthorhombic tunnel structure were synthesized by *chimie douce* ion exchange route. Small amount of Ti-doping was found to expand the lattice in $Li_{0.44}Mn_{0.89}Ti_{0.11}O_2$, thereby activating more facile Li^+ (de)insertion.

View Article Online
DOI: 10.1039/D5MA00455A

Thus, it led to improved discharge capacity of 129 mAh g^{-1} at a rate of C/20 along with superior Li^+ diffusivity, rate kinetics and cycling stability. The charge compensation occurred by solid solution (single-phase) redox mechanism. Hence, Ti-doping into tunnel-type $Li_{0.44}MnO_2$ can be adopted to improve electrochemical performance, particularly involving Jahn-Teller active Mn^{3+} species. Further, by varying the operating voltage window, anionic (oxygen) redox at high voltage and multiple cationic (Mn^{4+}/Mn^{3+} and Mn^{3+}/Mn^{2+}) redox at voltage below 2 V can be exploited in these Ti-doped $Li_{0.44}MnO_2$ cathode that will be reported shortly. Ti-doped $Li_{0.44}MnO_2$ possessing tunnel type framework can be harnessed as economic cathode for Li-ion batteries.

Data availability

The data supporting this article have been included as part of the Supplementary Information.

Acknowledgements

We acknowledge the financial support from the Department of Science and Technology (Govt. of India) under the aegis of Core Research Grant (CRG/2022/000963). J.Y., S.P.V., S.K.P. and N.D. thank the Ministry of Human Resource Development (MHRD, Govt. of India) for research fellowships. We acknowledge Prof. R.J. Deokate for help in manuscript preparation. J.Y. and N.D. are grateful to the Indo-French Laboratory for Solid-state Chemistry (LaFICS) for financial support to conduct internship at Normandie University, Caen, France. P.B. is grateful to the Alexander von Humboldt Fundation (Bonn, Germany) for a 2022 Humboldt fellowship for experienced researchers.

View Article Online
DOI: 10.1039/D5MA00455A

References

1. N. Ortiz-Vitoriano, N. E. Drewett, E. Gonzalo and T. Rojo, *Energy Environ. Sci.*, 2017, **10**, 1051–1074.
2. K. Zhang, X. Han, Z. Hu, X. Zhang, Z. Tao and J. Chen, *Chem. Soc. Rev.*, 2015, **44**, 699–728.
3. P. G. Bruce, A. R. Armstrong and H. Huang, *J. Power Sources*, 1997, **68**, 19–23.
4. A. Blyr, C. Sigala, G. Amatucci, D. Guyomard, Y. Chabre and J.-M. Tarascon, *J. Electrochem. Soc.*, 1998, **145**, 194–209.
5. A. R. Armstrong, H. Huang, R. A. Jennings and P. G. Bruce, *J. Mater. Chem.*, 1998, **8**, 255–259.
6. M. M. Doeff, A. Anapolsky, L. Edman, T. J. Richardson and L. C. De Jonghe, *J. Electrochem. Soc.*, 2001, **148**, A230–A236.
7. M. Zarrabeitia, E. Gonzalo, M. Pasqualini, M. Ciambezi, O. Lakuntza, F. Nobili, A. Trapananti, A. Di Cicco, G. Aquilanti, N. A. Katcho, J. M. López del Amo, J. Carrasco, M. Á. Muñoz-Márquez and T. Rojo, *J. Mater. Chem. A*, 2019, **7**, 14169–14179.
8. P. Zhan, K. Jiao, J. Wang, Z. Hu, R. Ma, H. Zhu and S. Jiao, *J. Electrochem. Soc.*, 2015, **162**, A2296–A2301.
9. G. Yang, H. Ni, H. Liu, P. Gao, H. Ji, S. Roy, J. Pinto and X. Jiang, *J. Power Sources*, 2011, **196**, 4747–4755.
10. A. Fukabori, H. Hayakawa, N. Kijima and J. Akimoto, *Electrochem. Solid-State Lett.*, 2011, **14**, A100–A103.
11. M. M. Doeff, T. J. Richardson and K. T. Hwang, *J. Power Sources*, 2004, **135**, 240–248.
12. J. Akimoto, J. Awaka, Y. Takahashi, N. Kijima, M. Tabuchi, A. Nakashima, H. Sakaebe and K. Tatsumi, *Electrochem. Solid-State Lett.*, 2005, **8**, A554–A557.
13. L. J. Hardwick, J. Saint, M. M. Doeff and R. Kostecki, *ECS Meet. Abstr.*, 2008, **MA2008-02**, 718.
14. J. Awaka, J. Akimoto, H. Hayakawa and Y. Takahashi, *J. Power Sources*, 2007, **174**, 1218–1223.
15. B. Li and D. Xia, *Adv. Mater.*, 2017, **29**, 1701054.
16. J. B. Goodenough and Y. Kim, *Chem. Mater.*, 2010, **22**, 587–603.
17. J. A. Saint, M. M. Doeff and J. Wilcox, *Chem. Mater.*, 2008, **20**, 3404–3411.

View Article Online
DOI: 10.1039/D5MA00455A

18. J. Rodríguez-Carvajal, *Phys. B*, 1993, **192**, 55–69.
19. K. Momma and F. Izumi, *J. Appl. Crystallogr.*, 2011, **44**, 1272–1276.
20. Y. Cao, L. Xiao, W. Wang, D. Choi, Z. Nie, J. Yu, L. V. Saraf, Z. Yang and J. Liu, *Adv. Mater.*, 2011, **23**, 3155–3160.
21. K. Dai, J. Mao, X. Song, V. Battaglia and G. Liu, *J. Power Sources*, 2015, **285**, 161–168.
22. W. J. Shi, D. Zhang, X. M. Meng, C. X. Bao, S. D. Xu, L. Chen, X. M. Wang, S. B. Liu and Y. C. Wu, *ACS Appl. Mater. Interfaces*, 2020, **12**, 14174–14184.
23. Y. Wang, J. Liu, B. Lee, R. Qiao, Z. Yang, S. Xu, X. Yu, L. Gu, Y.-S. Hu, W. Yang, K. Kang, H. Li, X.-Q. Yang, L. Chen and X. Huang, *Nat. Commun.*, 2015, **6**, 6401.
24. Z. Liu, W. G. Lin, K. W. Zhou and J. L. Yan, *Ceram. Int.*, 2018, **44**, 2797–2802.
25. U. Dutta, D. Ghosh, A. Haque, P. S. Walke, N. E. Mordvinova, O. I. Lebedev, K. Pal, A. Gayen, A. K. Kundu and M. M. Seikh, *J. Magn. Magn. Mater.*, 2018, **464**, 132–138.
26. U. Rizal, S. Das, D. Kumar, B. S. Swain and B. P. Swain, *AIP Conf. Proc.*, 2016, **1724**, 020135.
27. Z. Xiao, F. Xia, L. Xu, X. Wang, J. Meng, H. Wang, X. Zhang, L. Geng, J. Wu and L. Mai, *Adv. Funct. Mater.*, 2022, **32**, 2108244.
28. Y. Zhang, H. Xie, H. Jin, X. Li, Q. Zhang, Y. Li, K.F. Li, F. Luo, W. Li and C Li, *ACS Omega* 2021, **6**, 21304−21315.
29. M. C. Biesinger, B. P. Payne, A. P. Grosvenor, L. W. M. Lau, A. R. Gerson and R. S. C. Smart, *Appl. Surf. Sci.*, 2011, **257**, 2717–2730.
30. M. C. Biesinger, L. W. M. Lau, A. R. Gerson and R. S. C. Smart, *Appl. Surf. Sci.*, 2010, **257**, 887–898.
31. Y.-U. Park, R. A. Shakoor, K.-Y. Park and K.-S. Kang, *J. Electrochem. Sci. Technol.*, 2011, **2**, 14–19.
32. Y. S. Lee and K. S. Ryu, *Sci. Rep.*, 2017, **7**, 16617.

View Article Online
DOI: 10.1039/D5MA00455A

Data availability

The data supporting this article have been included as part of the Supplementary Information.